



# In situ coupled amorphous cobalt nitride with nitrogen-doped graphene aerogel as a trifunctional electrocatalyst towards Zn-air battery derived full water splitting

Haiyuan Zou<sup>a,b</sup>, Ge Li<sup>c</sup>, Lele Duan<sup>b,\*\*</sup>, Zongkui Kou<sup>a,d,\*</sup>, John Wang<sup>d</sup>

<sup>a</sup> School of Chemistry and Chemical Engineering, Harbin Institute of Technology, 92 west Da-Zhi Street, Harbin 150001, China

<sup>b</sup> Department of Chemistry and Shenzhen Grubbs Institute, Southern University of Science and Technology, Shenzhen, 518055, China

<sup>c</sup> Applied Physical Chemistry, Department of Chemistry, KTH Royal Institute of Technology, SE-10044 Stockholm, Sweden

<sup>d</sup> Department of Materials Science and Engineering, National University of Singapore, 117574, Singapore

## ARTICLE INFO

### Keywords:

Amorphous CoN<sub>x</sub>  
Nitrogen-doped graphene aerogel  
Water electrolysis  
Zinc-air battery  
Electrochemistry

## ABSTRACT

Herein, we report a new type of efficient trifunctional electrocatalyst by in situ coupling amorphous cobalt nitride (CoN<sub>x</sub>) nanoparticles within three-dimensional (3D) nitrogen-doped graphene aerogel (NGA). The CoN<sub>x</sub>/NGA nanohybrid with hierarchical porous structure guarantees the superior activities toward ORR, OER and HER, due to abundant dual active CoN<sub>x</sub> and N<sub>x</sub>C sites. Impressively, it also exhibits a long lifetime and exceptionally high electrochemical performances as a cathode and an anode in a two-electrode overall water splitting electrolyzer, and also as an air-cathode in a rechargeable Zn-air battery. In addition, the CoN<sub>x</sub>/NGA-based water splitting electrolyzer and two Zn-air batteries can be integrated together to effectively self-drive electrochemical water splitting device with high gas evolution rates of 186 and 372  $\mu\text{mol h}^{-1}$  for O<sub>2</sub> and H<sub>2</sub>, respectively. This work paves a way for designing advanced non-noble multifunctional catalysts, aiming for the real application of energy storage and conversion devices.

## 1. Introduction

Sustainable energy conversion and storage technologies via regenerative fuel cells, electrochemical water splitting and rechargeable metal-air batteries have the potential to mitigate the heavy reliance on global fossil fuels [1–3]. Generally, the oxygen reduction reaction (ORR), hydrogen evolution reaction (HER) and oxygen evolution reaction (OER) are considered as the three fundamental electrocatalytic reactions to achieve the above mentioned renewable energy strategies [4–6]. For instance, ORR and OER are two crucial reactions in metal-air batteries and fuel cells. Besides, OER and HER are two essential steps for the evolution of oxygen and hydrogen gases by water electrolysis [7–10]. Among these electrocatalytic processes, electrochemical oxidation and reduction of protons are mediated by appropriate catalysts which are applied to reduce the energy barrier and accelerate the reaction rate. Up to now, noble metals of Pt-based and Ir/Ru-based materials give prominent catalytic performances for ORR/HER and OER, respectively, while the low crustal abundance and the high cost of noble metals greatly hamper their extensive implementation. To this end,

substantial advances have directed toward nanostructuring or modulating the low-cost transition metal compounds that can expose additional active sites to substitute the precious metals [11–16].

Among available electrocatalyst candidates, transition metal nitrides (TMNs) with wide assortments of materials and tunable surface properties hold great promise for the development of highly efficient catalysts [17–20]. Especially, the cobalt-based TMNs have ignited particular interests owing to their tailored electronic structure of metal sites coordinated by N atoms and high intrinsic per-site catalytic activity [21–24]. For example, Xie et al. reported that metallic Co<sub>4</sub>N porous nanowire arrays activated by surface oxidation presented prominent OER performance [25]. Likewise, Shi et al. introduced a trace level of Co-N species into graphite foam to produce high dispersed active CoN<sub>x</sub> moieties, which rendered superior HER and OER activities [26]. Nevertheless, the rational design and synthesis of trifunctional catalysts that can simultaneously drive the ORR, OER and HER is desirable and challenging [27,28].

Given that morphological engineering can boost the catalytic properties of TMNs to some extent by increasing the surface area,

\* Corresponding author at: Department of Materials Science and Engineering, National University of Singapore, 117574, Singapore.

\*\* Corresponding author.

E-mail addresses: [duanll@sustc.edu.cn](mailto:duanll@sustc.edu.cn) (L. Duan), [msekz@nus.edu.sg](mailto:msekz@nus.edu.sg), [zongkuikou@whut.edu.cn](mailto:zongkuikou@whut.edu.cn) (Z. Kou).

metal-organic frameworks (MOFs) have been demonstrated as promising templates or precursors to construct diverse shapes of metal composites [29]. When prepared MOF as precursors, these catalysts feature for evenly and densely populated active sites around the electrode, expediently accessible by reactants [30]. For instance, various hollow or porous nanostructured MOFs derivatives of metal sulfides, phosphides and nitrides have been successfully built [31–34]. However, the consequent derivatives are inevitably agglomerated during preparation and catalytic processes, leading to reduced surface area and insufficient catalytic active sites. Recent breakthroughs have indicated that the incorporation of MOFs derivatives with carbonaceous materials such as graphene and carbon nanotubes, is a feasible method not only to prevent the aggregation of metal hosts but also to afford the resultant hybrids with improved electrocatalytic activity and stability by virtue of the excellent conductivity, large surface area and favorable electrochemical stability of carbon matrix [35–38]. One step forward is to fundamentally alter the intrinsic catalytic properties of the metal hosts, in which the highly disordered or amorphous materials have exhibited superior behaviors compared with their crystalline counterparts [39,40]. Although the mechanism of amorphous catalysts in promoting the electroactivity is still in dispute, two major functions are commonly accepted: (1) the tailored electronic properties are accomplished by amorphous materials, which optimize the adsorption energy of the reactants (e.g.,  $O_2/OH^-$ ); (2) the vacancy and coordinated structure of catalysts can expose more active sites and facilitate the catalytic kinetics [41,42].

Herein, we demonstrate an efficient and robust trifunctional electrocatalyst (denoted as  $CoN_x/NGA$ ) of amorphous  $CoN_x$  on a nitrogen-doped graphene aerogel (NGA) by using MOF as a precursor. The principles of catalyst design are as follows: (1) NGA acts as a 3D matrix to confine the MOF derivative from aggregation and thereby offers a highway to facilitate the electron transfer; (2) the amorphous structure of  $CoN_x$  particles and N-doped graphene frameworks provide abundant active  $CoN_x$  and  $N_xC$  sites to drive the electrochemical reactions; (3) the highly open 3D hierarchical architecture of the hybrid imparts the shortened pathway for mass transportation. The integrated advantages of  $CoN_x$  and NGA enable the  $CoN_x/NGA$  hybrid highly active toward ORR, OER and HER, the activities of which are comparable with precious metal catalysts. Notably, the overall water splitting electrolyzer using  $CoN_x/NGA$  as both a cathode and an anode achieves a current density of  $10\text{ mA cm}^{-2}$  at  $1.71\text{ V}$ , which is comparable to the  $RuO_2$  and  $Pt/C$  pair. The  $CoN_x/NGA$  is also incorporated into a rechargeable Zn-air battery, exhibiting a long-term stability and low discharging/charging overpotentials. Furthermore, we successfully used  $CoN_x/NGA$ -based Zinc-air batteries connected in series to drive our electrolyzer for realizing a self-driven electrochemical water splitting. This device can produce  $O_2$  and  $H_2$  gases at a rate of  $186$  and  $372\text{ }\mu\text{mol h}^{-1}$ , respectively, showing a great promise for practical applications.

## 2. Results and discussion

### 2.1. Synthesis and characterization of electrocatalysts

The strategy for synthesizing  $CoN_x/NGA$  nanohybrid is illustrated in Fig. S1. Firstly, the hierarchical porous graphene aerogel (GA) was prepared by introducing ascorbic acid to reduce graphene oxide (GO) and then conjugating reduced graphene sheets into a 3D graphene network. Subsequently, the obtained GA was immersed into a precursor solution to in situ grow the ZIF-67 (ZIF: zeolitic imidazolate framework) on the surface of GA. Finally, the resulting ZIF-67/GA was subjected to a tube furnace under thermal treatment at  $500\text{ }^\circ\text{C}$  under an ammonia atmosphere to form the target  $CoN_x/NGA$  hybrid. Bare  $CoN_x$  was also prepared as a reference, under otherwise identical protocols in the absence of GA. The morphology and microstructure of as-prepared samples were examined using scanning electron microscopy (SEM) and transmission electron microscopy (TEM). As shown in Fig. 1a, GA

presents a hierarchical porous graphene network structure, which could provide low-resistant diffusion channels for reaction intermediates, thereby contributing to the boosted electrochemical performance. The TEM images exhibit silk-like NGA with only 3 layers on the edge of the graphenes (graphene sheets), suggesting an ultrathin nature (Fig. S2a and b). Notably, the 3D highly porous architecture was well retained after in situ deposition of ZIF-67, implying the excellent ductility of NGA (Fig. 1b). The magnified SEM image (inset image of Fig. 1b) and energy-dispersive X-ray spectroscopy (EDXS) mapping images of ZIF-67/GA clearly show that the ZIF-67 nanocrystals are well-shaped with rhombic dodecahedral morphology and homogeneously anchored on the surface of NGA, indicating a strong interaction between these two components (Fig. S3a–e). After thermal treatment in  $NH_3$ , ZIF-67/GA was converted into  $CoN_x/NGA$ , well preserving the panoramic morphology of precursor (Fig. 1c) yet the anchored particles on graphene sheets shrank (inset Fig. 1c). The corresponding TEM image of  $CoN_x/NGA$  demonstrated that the initial rhombic dodecahedral ZIF-67 nanocrystals on NGA scaffold disappeared; instead, numerous nanoparticles were evenly decorated on the graphene sheets (Fig. 1d). Therefore, the ZIF-67 has undergone morphology and structure evolution under  $NH_3$  annealing, and  $NH_3$  was served as both a nitrogen source and etching gas. Additionally, the high-resolution TEM (HRTEM) image of  $CoN_x$  on NGA shows no obvious crystal lattice (Fig. 1e); the electron diffraction (SAED) pattern of the selected area presents vague diffraction rings, indicating an amorphous phase of  $CoN_x$  in the hybrid (Fig. 1f) [43]. Furthermore, the high angle annular dark field-scanning transmission electron microscopy (HAADF-STEM) and the associated EDS mapping images of  $CoN_x/NGA$  confirm the spatial distribution of C, N and Co elements on the composite (Fig. 1g–j), revealing the successful integration of  $CoN_x$  with NGA. Without the support of the porous NGA frame, ZIF-67 derived bare  $CoN_x$  is also synthesized as comparison, which presents a severe aggregation (Fig. S4a and b), thus impeding the electrolyte diffusion.

Fig. 2a displays the X-ray diffraction (XRD) patterns of the GA, ZIF-67, ZIF-67/GA, and their corresponding nitrated products (NGA,  $CoN_x$  and  $CoN_x/NGA$ ). A broad diffraction peak of GA and NGA is identified at  $20\text{--}30^\circ$  from the diffraction of reduced graphene sheets along their stacking direction and the framework of both samples constructed by few-layer stacked graphene sheets [44]. The XRD pattern of ZIF-67 is in line with the literature reported one [14]. The ZIF-67/GA shows a superimposition of GA phase and ZIF-67 phase, implying the successful incorporation of MOFs with GA. Notably, no obvious characteristic peaks of crystalline cobalt nitride can be detected in the XRD patterns of  $CoN_x$  or  $CoN_x/NGA$ , indicating their ultralow crystallinity after the  $NH_3$  calcination treatment. On the other hand, the surface area and pore size distribution of the above three thermally annealed products were investigated by  $N_2$  adsorption-desorption isotherms (Fig. 2b). All these samples exhibit the type IV  $N_2$  sorption curves, which imply mesopores within them. The Brunauer-Emmett-Teller (BET) surface area and pore volume of  $CoN_x/NGA$  were calculated as  $227\text{ m}^2\text{ g}^{-1}$  and  $0.41\text{ m}^3\text{ g}^{-1}$ , respectively, which are much larger than those of bare  $CoN_x$  ( $28\text{ m}^2\text{ g}^{-1}$ ,  $0.08\text{ m}^3\text{ g}^{-1}$ ) (Table 1). Notably, the pore size distribution curve of  $CoN_x/NGA$  shows bimodal pore-size distribution, which confirms the presence of both mesopores (peak pore at ca.  $4\text{ nm}$ ) and macropores (peak pore at ca.  $60\text{ nm}$ ) in the sample (inset image of Fig. 2b). Besides, the extremely large hundred-micrometer-size pores constructed by the graphene scaffolds can also be detected in the sample according to aforementioned SEM images. As a result, such hierarchical pore structure of  $CoN_x/NGA$  associated with large surface area can offer abundant catalytic active sites with smooth mass transportation. Furthermore, the Raman spectrum of  $CoN_x/NGA$  was also collected and compared with ZIF-67/GA and the GO raw material. As shown in Fig. 2c, there are mainly two Raman scattering peaks at ca.  $1356$  and  $1587\text{ cm}^{-1}$ , corresponding to the disorder carbon (D-band) and graphitic carbon (G-band), respectively [45,46]. The relative intensity of D to G-band ( $I_D/I_G$ ) is a paramount index of defect degree of carbon nanomaterials

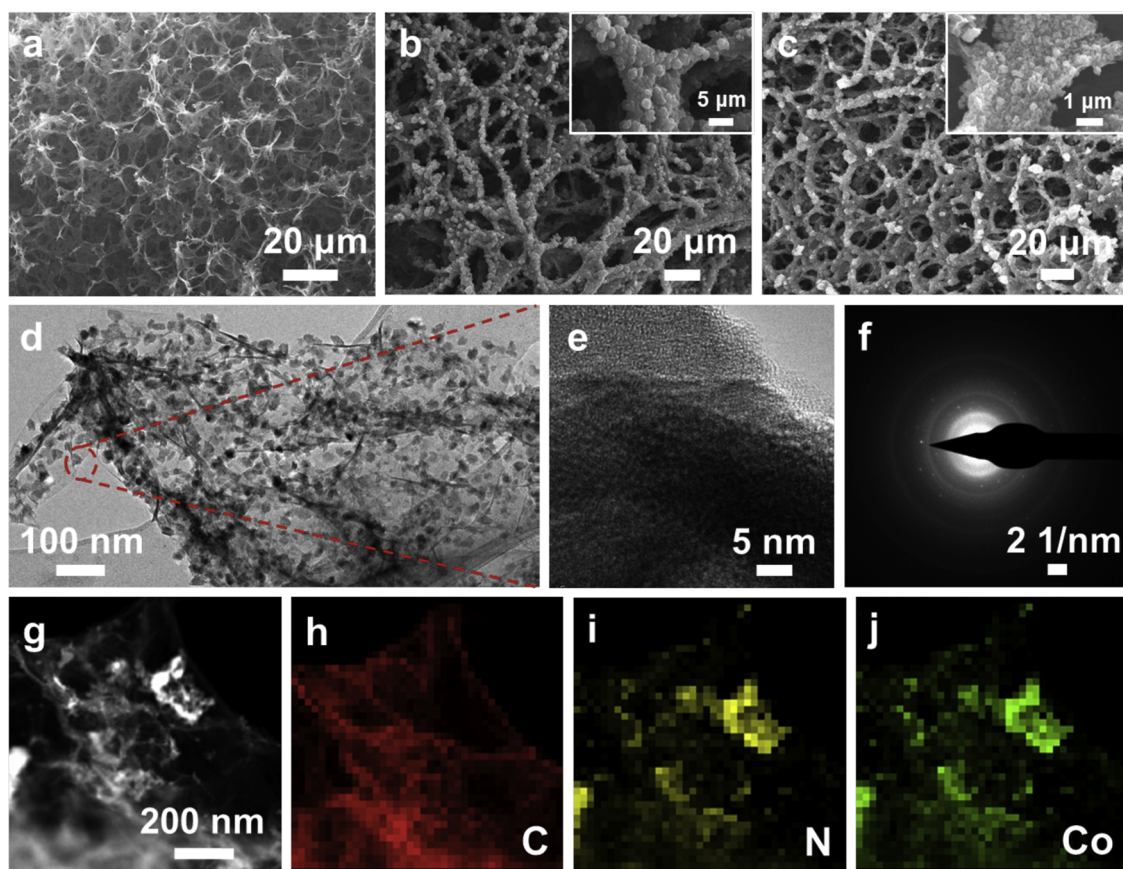


**Fig. 1.** Panoramic SEM images of (a) GA, (b) ZIF-67/GA and (c) CoN<sub>x</sub>/NGA. (Inset: the high-magnification SEM images of the samples) (d) TEM image, (e) HRTEM image, (f) SAED pattern, (g) HAADF, (h–j) EDXS images of CoN<sub>x</sub>/NGA.

[47,48]. The intensity ratio shows an increased trend in the order of GO (1.06) < ZIF-67/GA (1.47) < CoN<sub>x</sub>/NGA (1.83), revealing that more defects were generated with the NH<sub>3</sub> treatment through the etching and doping effects. The defects on the NGA can also function as catalytic active sites and favor the electrocatalytic processes.

X-ray photoelectron spectroscopy (XPS) spectra were recorded to investigate the bonding configurations of N and the chemical states of the elements. As shown in Fig. 3a, the XPS signals at around 285 eV, 400 eV, 531 eV and 782 eV are respectively corresponding to C 1s, N 1s, O 1s and Co 2p. The high-resolution N 1s of CoN<sub>x</sub>/NGA can be deconvoluted into four N species, namely, Co-N (399.3 eV), pyridinic-N (398.15 eV), pyrrolic-N (400.59 eV) and graphitic-N (401.79 eV), respectively and all these N species are well documented to facilitate the electrocatalytic process (Fig. 3b) [49–51]. In particular, the Co-N<sub>x</sub> species has been demonstrated as one of the most efficient active sites for ORR and HER [52,53]. In contrast, only pyridinic-N, pyrrolic-N and graphitic-N signals were observed in the N 1s spectrum of NGF without the Co-N one (Fig. S5a). In the Co 2p spectrum, Co 2p<sub>3/2</sub> and Co 2p<sub>1/2</sub> located at around 780 and 795 eV respectively along with their satellite (Sat.) peaks at 790 and 804 eV (Fig. 3c) [54]. By deconvolution, two distinguished Co species can be identified, where Co<sup>2+</sup> (Co-N<sub>y</sub>) fitting peak centered at 780.5 eV, and Co<sup>3+</sup> (CoC<sub>x</sub>N<sub>y</sub>) fitting peak centered at 782 eV (Fig. S5b) [55]. The Co<sup>3+</sup>/Co<sup>2+</sup> ratio is calculated to be 1.21, and the high valent states of Co is believed as a major contributor to OER [56]. On the basis of these advancements, CoN<sub>x</sub>/NGA is anticipated as a cost-effective and efficient trifunctional catalyst for HER, OER and ORR.

## 2.2. Catalytic properties for ORR

The ORR process, as a paramount role in a variety of fuel cells and

metal-air batteries, is first assessed to reveal the potential of CoN<sub>x</sub>/NGA in electrocatalysis. The catalyst loading on the rotating disk electrode (RDE) is 0.21 mg cm<sup>-2</sup>. Cycle voltammetry (CV) of CoN<sub>x</sub>/NGA (Fig. 4a) was studied in N<sub>2</sub> or O<sub>2</sub>-saturated 0.1 M KOH solutions. Under N<sub>2</sub> atmosphere, CoN<sub>x</sub>/NGA displays a broad reduction peak at ca. 0.6 V due to the reduction of cobalt species; a characteristic oxygen reduction peak at ~ 0.78 V was identified for the CoN<sub>x</sub>/NGA in O<sub>2</sub>-saturated electrolyte, and in contrast no current enhancement was observed under N<sub>2</sub> atmosphere. The linear sweep voltammetry (LSV) curves were recorded on a RDE with a rotation rate of 1600 rpm to estimate the ORR performance of our samples and the benchmark of commercial Pt/C electrocatalyst (Fig. 4b). Both the onset potential (0.93 V) and the half-wave potential (E<sub>1/2</sub>, 0.83 V) for CoN<sub>x</sub>/NGA are close to those of the noble metal benchmark Pt/C (onset potential: 0.96 V, E<sub>1/2</sub>: 0.85 V), and superior to bare CoN<sub>x</sub> (onset potential: 0.78 V, E<sub>1/2</sub>: 0.66 V) and NGA (onset potential: 0.7 V, E<sub>1/2</sub>: 0.54 V). Moreover, the CoN<sub>x</sub>/NGA renders a diffusion-limited current density (E<sub>j</sub>, 5.4 mA cm<sup>-2</sup>) as high as Pt/C, highlighting its prominent ORR response. The LSV curves of CoN<sub>x</sub>/NGA at various rotating rates exhibit a similar waveform (Fig. 4c), with a constant kinetic current slope. Owing to the faster diffusion process at higher rotating speed, an increased current with increasing rotation speed was observed for all samples (Fig. S6a–d). As depicted in Fig. 4d, Tafel slopes for NGA (121.5 mV dec<sup>-1</sup>) and CoN<sub>x</sub> (88.3 mV dec<sup>-1</sup>) are much higher than that of CoN<sub>x</sub>/NGA (65.8 mV dec<sup>-1</sup>), revealing a more favorable ORR kinetics of the later, which is due to the combined advantages of efficient CoN<sub>x</sub> catalyst with highly conductive NGA with abundant edge defects. The linear Koutecky-Levich (K-L) plots for CoN<sub>x</sub>/NGA prove the first-order reaction kinetics with respect to the dissolved oxygen concentration and similar electron transfer numbers (n) at various potentials (Fig. S7). The value of n is calculated to be in the range of 4.03–4.22 for the potential range of 0.3–0.7 V, indicating a



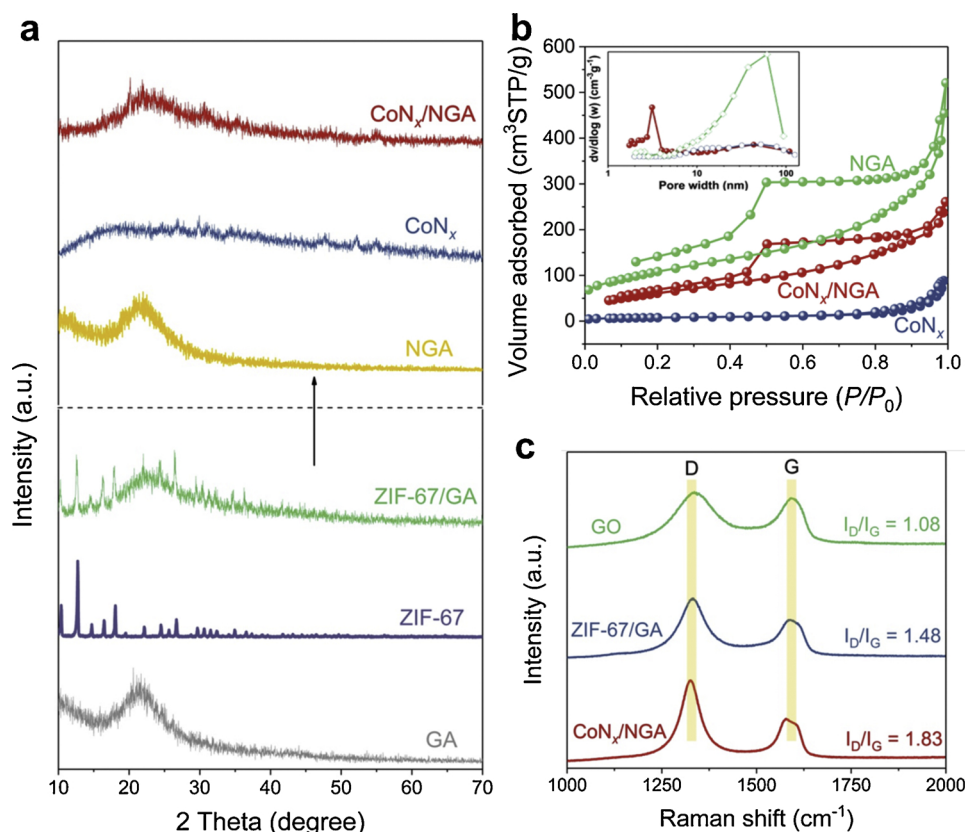


**Fig. 2.** (a) XRD patterns of GA, ZIF-67, ZIF-67/NGA and their derived products. (b) N<sub>2</sub> sorption isotherms (the inset is the corresponding pore size distribution) of NGA, CoN<sub>x</sub>, and CoN<sub>x</sub>/NGA. (c) Raman spectra of GO, ZIF-67/GA, and CoN<sub>x</sub>/NGA.

**Table 1**

Physical properties of the as-prepared samples.

Samples	$S_{\text{BET}}$ ( $\text{m}^2 \text{g}^{-1}$ )	$V_{\text{pore}}$ ( $\text{m}^3 \text{g}^{-1}$ )	$d_{\text{pore}}$ (nm)
NGA	393	0.58	5.8
CoN <sub>x</sub>	28	0.08	12.3
CoN <sub>x</sub> /NGA	227	0.41	7.1

near-four electron pathway. Additionally, rotating ring-disk electrode (RRDE) technique was also employed to monitor the amount of H<sub>2</sub>O<sub>2</sub> production during ORR process (Fig. 4e). The ratio of the undesirable HO<sub>2</sub><sup>−</sup> generation at CoN<sub>x</sub>/NGA electrode has a low percentage (< 5%), revealing a high selectivity of CoN<sub>x</sub>/NGA for four electron pathway (Fig. 4f). Based on the RRDE tests, the value of *n* for the CoN<sub>x</sub>/NGA is calculated to be 4.05–4.13, which is consistent with the corresponding results obtained from K-L curves. Furthermore, chronoamperometric response of CoN<sub>x</sub>/NGA and Pt/C was performed in O<sub>2</sub>-saturated 0.1 M KOH solution at -0.5 V (versus Ag/AgCl) with 1600 rpm (Fig. 5f). After continuous operation for 10 h, CoN<sub>x</sub>/NGA still retains good stability with a slow current attenuation and 89% retention, while Pt/C electrode shows a loss of more than 33% initial activity under the same condition, indicating NGA can well stabilize high dispersed CoN<sub>x</sub> by preventing the aggregation of CoN<sub>x</sub> particles. These advantages of CoN<sub>x</sub>/NGA show comparable or even better catalytic activity than the recent reported high active ORR electrocatalysts [57].

In order to further elucidate the effects of NH<sub>3</sub> calcination on ORR performance, we annealed the ZIF-67/GA under N<sub>2</sub> atmosphere to derive Co/GA. Unfortunately, the Co/GA gives an onset potential of 0.82 V, an *E*<sub>1/2</sub> of 0.71 V and an *E*<sub>j</sub> of 4 mA cm<sup>−2</sup> (Fig. S8). The overall performance of Co/GA is much worse than that of CoN<sub>x</sub>/NGA, which firmly indicates the NH<sub>3</sub> thermal treatment plays an essential role in modulating the catalytic activity of MOF-derivatives. Going one step

further, the pristine ZIF-67/GA was heated under NH<sub>3</sub> atmosphere at 400 °C and 600 °C, and the resulting catalysts were labeled as CoN<sub>x</sub>/NGA-400 and CoN<sub>x</sub>/NGA-600, respectively. Both CoN<sub>x</sub>/NGA-400 (onset potential: 0.89 V, *E*<sub>1/2</sub>: 0.82 V, and *E*<sub>j</sub>: 4.7 mA cm<sup>−2</sup>) and CoN<sub>x</sub>/NGA-600 (onset potential: 0.88 V, *E*<sub>1/2</sub>: 0.81 V, and *E*<sub>j</sub>: 5.0 mA cm<sup>−2</sup>) show suboptimal activity than the CoN<sub>x</sub>/NGA which underwent 500 °C NH<sub>3</sub> treatment (Fig. S9a and b). The TEM image of CoN<sub>x</sub>/NGA-400 °C presented insufficient NH<sub>3</sub> etching under low temperature, yielding aggregated CoN<sub>x</sub> particles on NGA (Fig. S9c). As the temperature is further increased to 600 °C, the CoN<sub>x</sub> particles are over corroded, where the scattered particles are decorated on NGA (Fig. S9d). Even so, all three samples prepared at different temperatures still consistently display superior ORR performance than the Co/GA, suggesting the NH<sub>3</sub> treatment can intrinsically change the catalytic properties of the hybrids. Overall, the above results guarantee the potential of CoN<sub>x</sub>/NGA in the field of ORR electrocatalysis and ensures its capability as a non-noble but efficient electrocatalyst for practical applications.

### 2.3. Water splitting performance

We then evaluated the electrocatalytic activity of as prepared CoN<sub>x</sub>/NGA on nickel foam for OER and HER. The catalysts loading on the nickel foam is 1 mg cm<sup>−2</sup>. Water splitting electrolysis was performed in 1.0 M KOH electrolyte with a slow scan rate of 5 mV s<sup>−1</sup>, and polarization curves were displayed without *iR* correction. Fig. 5a presents the LSV curves of NGA, CoN<sub>x</sub>, CoN<sub>x</sub>/NGA, and commercial RuO<sub>2</sub> benchmark on nickel foam towards OER. Clearly, the CoN<sub>x</sub>/NGA exhibits a small onset potential around 278 mV with a rapidly rising anodic current as more positive potential is applied. To achieve the benchmark current density of 10 mA cm<sup>−2</sup> (Fig. 5b), the CoN<sub>x</sub>/NGA requires a low overpotential (*η*<sub>10</sub>) of 295 mV, which is superior to that of the bare CoN<sub>x</sub> (371 mV), NGA (472 mV) and commercial RuO<sub>2</sub> (331 mV),

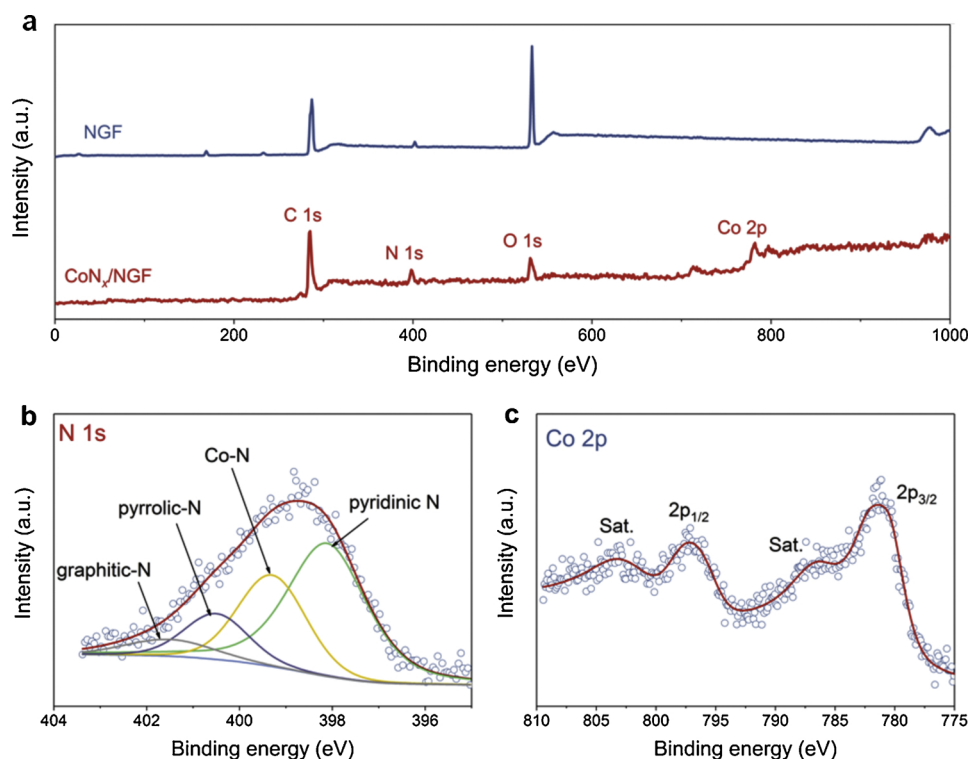


Fig. 3. (a) XPS survey spectra of NGA and CoN<sub>x</sub>/NGA. High-resolution XPS profiles of (b) N 1s, (c) Co 2p of CoN<sub>x</sub>/NGA.

demonstrating the positive interplay of CoN<sub>x</sub> and NGA in CoN<sub>x</sub>/NGA hybrid for OER. The pronounced electrocatalytic activity of CoN<sub>x</sub>/NGA electrocatalyst can be verified by a small Tafel slope of 82.3 mV dec<sup>-1</sup>, which is lower than those of CoN<sub>x</sub> (112.5 mV dec<sup>-1</sup>), NGA (166.3 mV dec<sup>-1</sup>), and RuO<sub>2</sub> (91.4 mV dec<sup>-1</sup>), indicating the facile catalytic reaction kinetics of the hybrid (Fig. 5c). Likewise, the electrocatalytic HER activities of these catalysts were tested in 1 M KOH as well (Fig. 5d). Analogously, CoN<sub>x</sub>/NGA shows impressive HER performance, which only needs an overpotential of  $\eta_{10} = 198$  mV to achieve the current density of 10 mA cm<sup>-2</sup>. This value is higher than that of precious metal-based Pt/C (55 mV), but much lower than that of CoN<sub>x</sub> (258 mV) and NGA (302 mV) (Fig. 5e). Notably, a relatively small Tafel slope of 97.3 mV dec<sup>-1</sup> was observed for CoN<sub>x</sub>/NGA (Fig. 5f), in comparison with 156.2 and 192.4 mV dec<sup>-1</sup> for CoN<sub>x</sub> and NGA, respectively, disclosing a faster HER response of CoN<sub>x</sub>/NGA. The durability of CoN<sub>x</sub>/NGA toward OER and HER was assessed under constant current density of 10 mA cm<sup>-2</sup> and -10 mA cm<sup>-2</sup>, respectively. As shown by the chronopotentiometry curves (Fig. 5g), the potential of CoN<sub>x</sub>/NGA for both OER and HER remains nearly constant under the continuous, long-term electrolysis reaction, suggesting the excellent stability of CoN<sub>x</sub>/NGA.

To step closer to the real application, overall water splitting in a two-electrode electrochemical cell was studied, in which two pieces of identical CoN<sub>x</sub>/NGA-loaded nickel foams were served as the anode and cathode. In a control experiment, the benchmark assembly of hybrid Pt/C + RuO<sub>2</sub> loaded on nickel foams was also investigated for comparison. It is worth noting that on OER profile, CoN<sub>x</sub> may undergo superficial or complete transformation into metal oxides and/or (oxy)hydroxides during the OER process, and the formed oxide species on the were responsible for the OER [58]. As the result, “bifunctional” is laden with double quotes to represent the converted precursor on the water oxidation side in overall water splitting in our case. From the polarization curves (Fig. 6a), the CoN<sub>x</sub>/NGA-based electrolyzer shows nearly the

same performance as the one constructed by RuO<sub>2</sub> + Pt/C, with a current density of 10 mA cm<sup>-2</sup> reached by applying just 1.71 V across the two electrodes. Furthermore, CoN<sub>x</sub>/NGA exhibits a negligible potential shift at galvanostatic test at 10 and 30 mA cm<sup>-2</sup> current densities for a long period of 22 h, confirming the good stability of CoN<sub>x</sub>/NGA as a “bifunctional” electrocatalyst for water splitting. With excellent bifunctionality, durability and cost-effectiveness, the CoN<sub>x</sub>/NGA catalyst holds great promise for electrocatalytic applications.

#### 2.4. Application on zinc-air batteries

Further, a proof-of-concept test was carried out to demonstrate the feasibility of CoN<sub>x</sub>/NGA in a rechargeable Zn-air battery. Since ORR and OER are essential steps in the discharging and charging processes of Zn-air batteries, CoN<sub>x</sub>/NGA is highly promising for rechargeable Zn-air batteries. As shown in Fig. 7a, a homemade Zn-air battery was constructed with zinc plate as the anode, CoN<sub>x</sub>/NGA as the air cathode with the catalyst loading of 1 mg cm<sup>-2</sup>, and 6 M KOH with 0.2 M zinc acetate as the electrolyte. For comparison, the Pt/C and RuO<sub>2</sub> blended catalyst with the same proportion (Pt/C + RuO<sub>2</sub>) was served as the rechargeable noble metal-air cathode. The battery assembled by CoN<sub>x</sub>/NGA can work smoothly with a high open-circuit of 1.33 V (Fig. 7b), which is close to that of the RuO<sub>2</sub> + Pt/C as the air cathode (1.35 V). Moreover, low overpotentials are observed for CoN<sub>x</sub>/NGA during the discharging/charging process (Fig. 7c), which could be mainly ascribed to the preferable ORR/OER performance of CoN<sub>x</sub>/NGA. It is known that a minimal overpotential region for discharge and charge potential is favorable for practical applications [59]. For comparison, at a current density of 50 mA cm<sup>-2</sup>, the potential gap of discharging (0.97 V) and charging (1.76 V) for CoN<sub>x</sub>/NGA-based battery is 0.79 V, which was 0.12 V lower than that of the precious metal-based one. Additionally, CoN<sub>x</sub>/NGA yields a gravimetric energy density of 638 Wh kg<sup>-1</sup>, which is comparable to the performance of RuO<sub>2</sub> + Pt/C (662 Wh kg<sup>-1</sup>) and

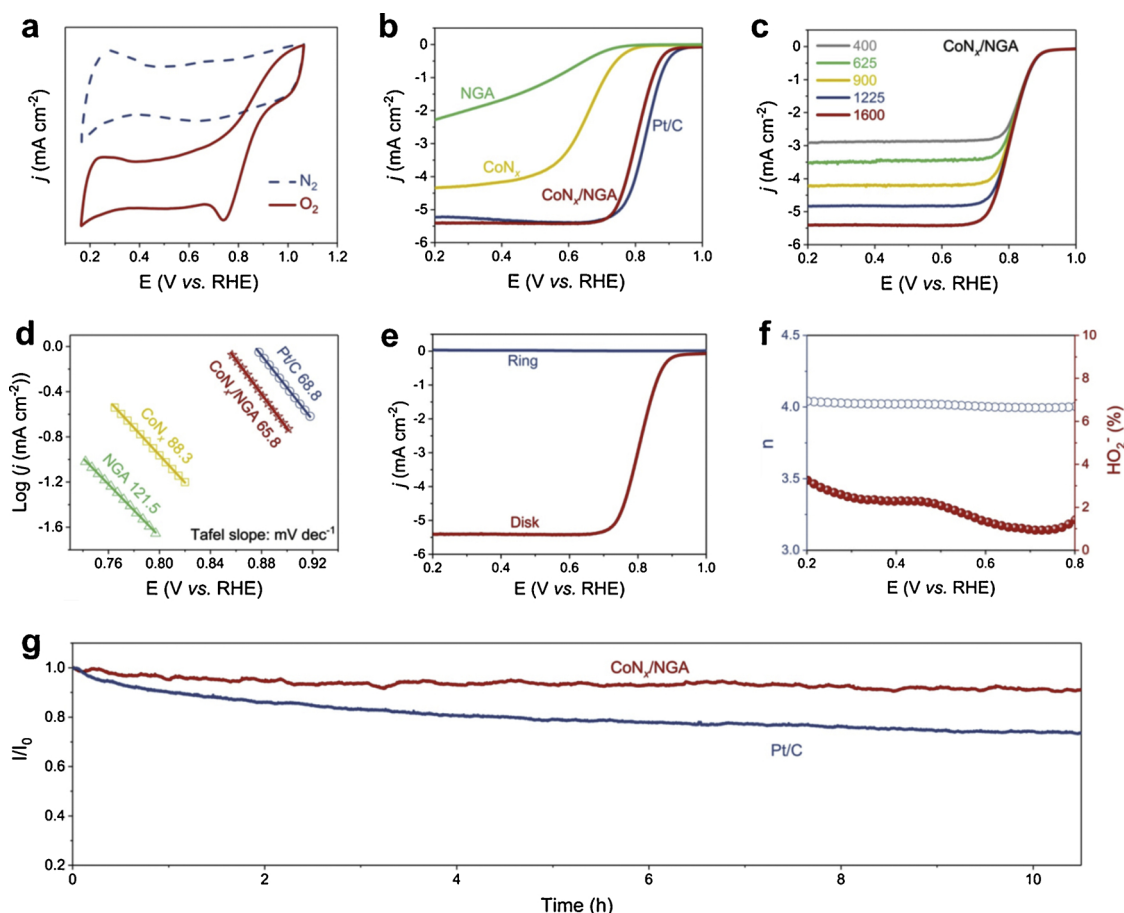


**Fig. 4.** (a) CV curves of Co<sub>N<sub>x</sub></sub>/NGA in N<sub>2</sub>- and O<sub>2</sub>-saturated 0.1 M KOH solution at a scan of 50 mV s<sup>-1</sup>. (b) LSV curves at a rotational speed of 1600 rpm for Co<sub>N<sub>x</sub></sub>, NGA, Co<sub>N<sub>x</sub></sub>/NGA, and Pt/C with a scan rate of 5 mV s<sup>-1</sup> in 0.1 M KOH solutions. (c) LSV curves for Co<sub>N<sub>x</sub></sub>/NGA at various rotating speeds (d) Tafel plots of oxygen reduction catalysts. (e) RRDE curve for Co<sub>N<sub>x</sub></sub>/NGA at a rotation speed of 1600 rpm in 0.1 M KOH solutions. (f) Electron transfer numbers and peroxide yields of Co<sub>N<sub>x</sub></sub>/NGA electrode at different potentials based on RRDE data. (g) Chronoamperometric response of Co<sub>N<sub>x</sub></sub>/NGA and Pt/C in O<sub>2</sub>-saturated 0.1 M KOH at -0.5 V (vs. Ag/AgCl) and 1600 rpm.

makes it a very competitive alternative of noble metal-based catalysts for Zinc-air batteries (Fig. 7d). Furthermore, the cycling measurement was performed at 10 mA cm<sup>-2</sup> to assess the rechargeability of the batteries. Like RuO<sub>2</sub> + Pt/C, Co<sub>N<sub>x</sub></sub>/NGA displays impressively negligible potential fading after 12 h charge-discharge test (Fig. 7e), implying its ultrahigh catalytic durability. Finally, the Co<sub>N<sub>x</sub></sub>/NGA-based battery can power an electric fan for around 5 h, showing its practical application value.

Despite reactions of ORR, OER and HER are different in terms of working principles, there are general criterions for designing active electrocatalysts for these reactions, such as large active surface area, excellent electrical conductivity and short diffusion pathway, etc. The Co<sub>N<sub>x</sub></sub>/NGA nanohybrid fulfills these criterions due to its unique structural merits. Firstly, the hierarchical porous NGA can serve as a 3D matrix and a highway for a fast charge transfer. Moreover, the whole network architecture could prevent the Co<sub>N<sub>x</sub></sub> nanostructures from corrosion, detachment and electrical isolation, rendering high stability for continuous electrochemical operating. Second, the homogeneously distributed amorphous Co<sub>N<sub>x</sub></sub> on NGA not only ensures a high surface area with abundant active sites for electrochemical reactions, but also imparts the extremely shortened pathway for mass diffusion and charge transfer. Finally, the highly opened 3D hierarchical architecture with the subunits of ultrasmall dimension possesses intrinsic advantages over

aggregated nanoparticles and 1D counterparts owing to superior electric contact and fast ionic transport across large and continuous active surface. On the basis of these premises, outstanding electrochemical activity and stability are achieved by Co<sub>N<sub>x</sub></sub>/NGA nanohybrid. In fact, the Co<sub>N<sub>x</sub></sub>/NGA also show advantages over many other trifunctional catalysts in terms of the major performance parameters [60–63].

## 2.5. Self-driven electrochemical overall water splitting

Meriting by the above-demonstrated excellent electrocatalytic activity of overall water splitting and zinc-air battery, an integrated self-driven water splitting unit based on Co<sub>N<sub>x</sub></sub>/NGA was then assembled. The schematic diagram of the device is presented in Fig. 8a. Since the onset potential of Co<sub>N<sub>x</sub></sub>/NGA-based overall water splitting cell is 1.61 V (Fig. 6a) and the open-circuit potential of Co<sub>N<sub>x</sub></sub>/NGA air-cathode based zinc-air battery is 1.33 V, two zinc-air batteries connected in series are enough to power the overall water splitting device. Two zinc-air batteries in series work at a constant open-circuit potential of 2.53 V (Fig. S12). Thereby two Co<sub>N<sub>x</sub></sub>/NGA air-cathode based zinc-air batteries were connected to drive the wired water splitting electrolyzer where two pieces of Co<sub>N<sub>x</sub></sub>/NGA-coated nickel foam were served as electrodes for O<sub>2</sub> and H<sub>2</sub> evolution (Fig. S13). The gases generated were quantified by means of gas chromatography (GC), and the plots of gas volume as a

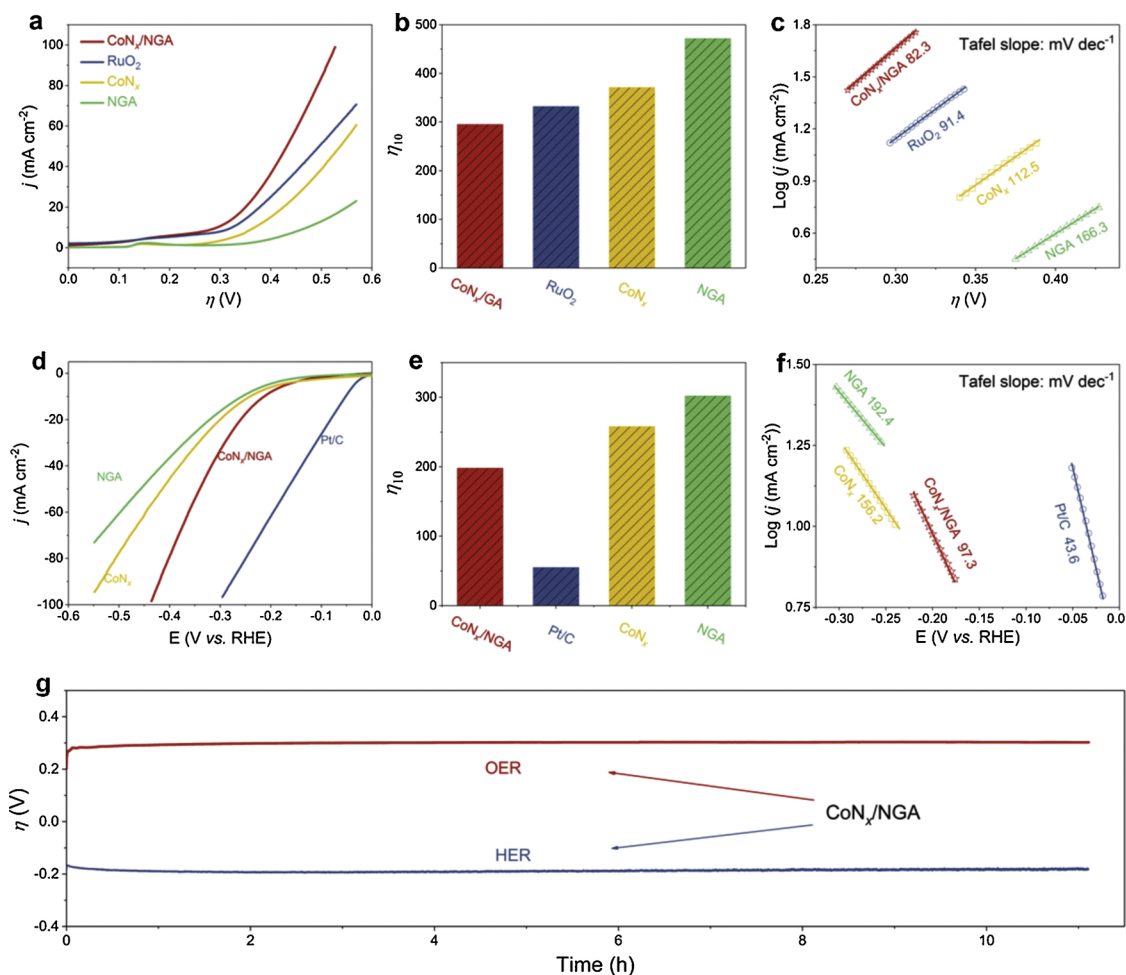


**Fig. 5.** (a) LSV curves, (b)  $\eta_{10}$ , and (c) Tafel plots of CoNx, NGA, CoNx/NGA, and RuO<sub>2</sub> for OER; (d) LSV curves, (e)  $\eta_{10}$ , and (f) Tafel plots of prepared catalysts and Pt/C for HER in 1 M KOH solutions at a scan rate of 5 mV s<sup>-1</sup>. (g) Long-term stability carried out at 10 and -10 mA cm<sup>-2</sup>.

function of time are given in Fig. 8c. The molar ratio of evolved O<sub>2</sub> to H<sub>2</sub> was close to the anticipated 1:2 stoichiometry (within experimental error) for overall water splitting, and the average O<sub>2</sub> and H<sub>2</sub> evolution rates are 186  $\mu\text{mol h}^{-1}$  and 372  $\mu\text{mol h}^{-1}$ , respectively.

### 3. Conclusion

In summary, a novel trifunctional hybrid catalyst of CoNx anchored on the nitrogen-doped graphene aerogel has been successfully developed. The CoNx/NGA catalyst inherits the prominent catalytic activity of CoNx and the excellent conductivity of NGA, and consequently

exhibits exceptional performance towards ORR, OER and HER. Furthermore, CoNx/NGA is applied as a “bifunctional” catalyst in two-electrode overall water splitting electrolyzer and as an air cathode for a rechargeable zinc-air battery; it is noteworthy that the excellent activity and stability of CoNx/NGA are comparable to those of highly active noble-metal catalysts. Two CoNx/NGA-based zinc-air batteries connected in series is able to drive a CoNx/NGA-based water splitting device to produce O<sub>2</sub> and H<sub>2</sub> at the rate of 186 and 372  $\mu\text{mol h}^{-1}$ , respectively, highlighting its potential application as efficient and low-cost energy storage devices.

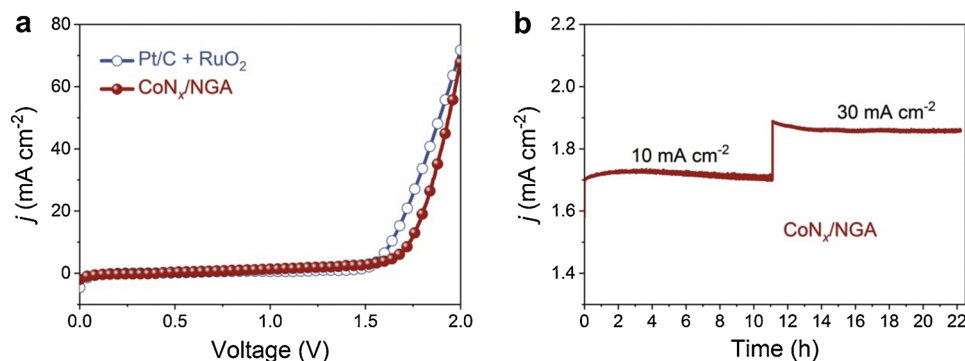


**Fig. 6.** (a) CoNx/NGA for overall water splitting in a two-electrode configuration with 1 M KOH as electrolyte and a scan rate of 5 mV s<sup>-1</sup>. (b) Chronopotentiometry test at 10 and 30 mA cm<sup>-2</sup>.



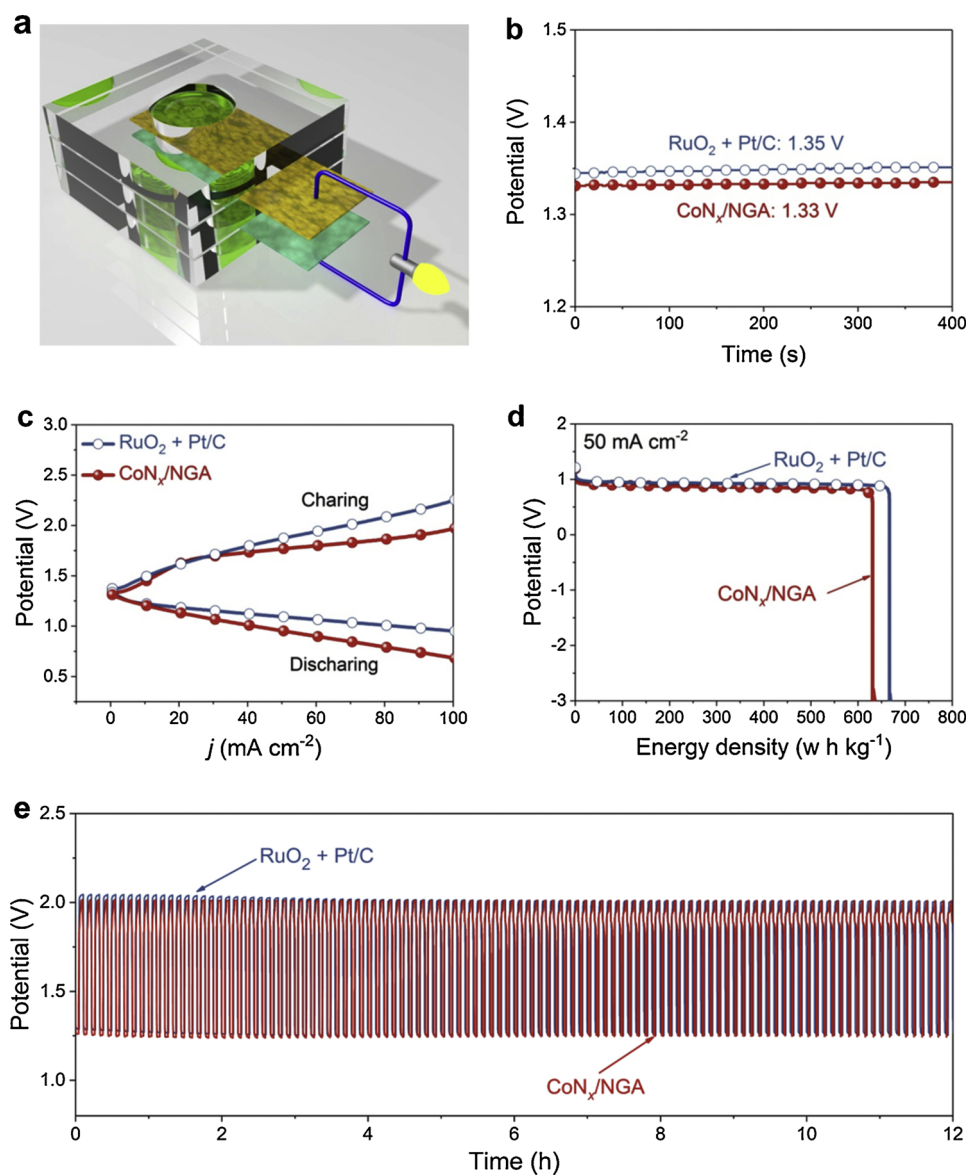


**Fig. 7.** Zinc-air battery performance of CoN<sub>x</sub>/NGA acting as the air cathode in comparison with the noble metal RuO<sub>2</sub> + Pt/C catalyst. (a) Schematic illustration of a rechargeable Zn-air battery. (b) Open-circuit plots. (c) Charging and discharging polarization curves. (d) Energy density plots at 50 mA cm<sup>-2</sup>. (e) Long-term cycling performance at 10 mA cm<sup>-2</sup>.

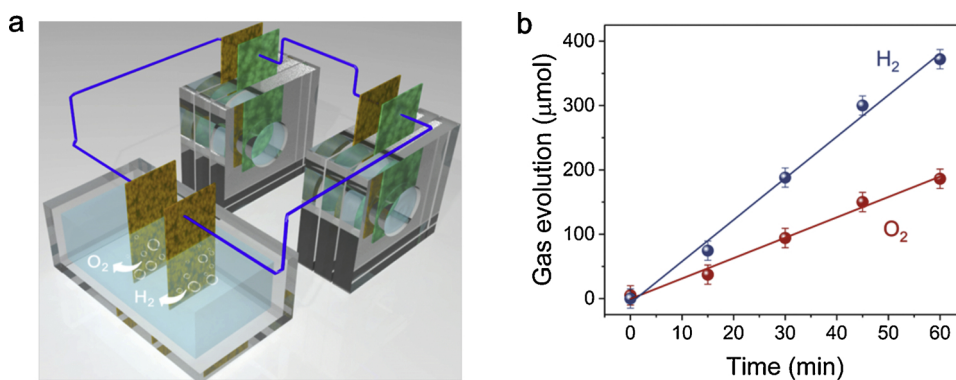


**Fig. 8.** (a) Scheme of the structure characterization of the self-driven overall water splitting device. (b) Oxygen and hydrogen evolution rates in the integrated device.



## Declaration of Competing Interest

The authors declare no competing financial interest.

## Acknowledgements

This work is supported by the National Natural Science Foundation of China (21771098), the Science and Technology Innovation Commission of Shenzhen Municipality (JCYJ20170817111548026) and the Shenzhen Nobel Prize Scientists Laboratory Project (C17783101).

## Appendix A. Supplementary data

Supplementary material related to this article can be found, in the online version, at doi:<https://doi.org/10.1016/j.apcatb.2019.118100>.

## References

- [1] Z.W. Seh, J. Kibsgaard, C.F. Dickens, I.B. Chorkendorff, J.K. Nørskov, T.F. Jaramillo, Combining theory and experiment in electrocatalysis: insights into materials design, *Science* 355 (2017) 6321, <https://doi.org/10.1126/science.aad4998>.
- [2] H. Li, Q. Li, P. Wen, T.B. Williams, S. Adhikari, C. Dun, C. Lu, D. Itanze, L. Jiang, D.L. Carroll, G.L. Donati, P.M. Lundin, Y. Qiu, S.M. Geyer, Colloidal cobalt phosphide nanocrystals as trifunctional electrocatalysts for overall water splitting powered by a zinc-air battery, *Adv. Mater.* 30 (2018) 1705796, <https://doi.org/10.1002/adma.201705796>.
- [3] R. Xiang, Y. Duan, L. Peng, Y. Wang, C. Tong, L. Zhang, Z. Wei, Three-dimensional core@shell Co@CoMoO<sub>4</sub> nanowire arrays as efficient alkaline hydrogen evolution electrocatalysts, *Appl. Catal. B-Environ.* 246 (2019) 41–49, <https://doi.org/10.1016/j.apcatb.2019.01.035>.
- [4] J. Yang, X. Wang, B. Li, L. Ma, L. Shi, Y. Xiong, H. Xu, Polypyrrole hydrogel-derived trifunctional electrocatalyst for self-powered overall water splitting, *Adv. Funct. Mater.* 27 (2017) 1606497, <https://doi.org/10.1002/adfm.201606497>.
- [5] C.W. Cheung, X. Hu, Amine synthesis via iron-catalysed reductive coupling of nitroarenes with alkyl halides, *Nat. Commun.* 7 (2016) 12494, <https://doi.org/10.1038/ncomms12494>.
- [6] Q. Wang, K. Dastafkan, C. Zhao, Design strategies for non-precious metal oxide electrocatalysts for oxygen evolution reactions, *Curr. Opin. Electrochem.* 10 (2018) 16–23, <https://doi.org/10.1016/j.coelec.2018.03.015>.
- [7] J. Zhang, L. Dai, Phosphorus, and fluorine tri-doped graphene as a multifunctional catalyst for self-powered electrochemical water splitting, *Angew. Chem. Int. Ed.* 55 (2016) 13296–13300, <https://doi.org/10.1002/anie.201607405>.
- [8] P. Liu, D. Gao, W. Xiao, L. Ma, K. Sun, P. Xi, D. Xue, J. Wang, Self-powered water-splitting devices by core-shell NiFe@N-graphite-based Zn-air batteries, *Adv. Funct. Mater.* 28 (2018) 1706928, <https://doi.org/10.1002/adfm.201706928>.
- [9] J. Duan, S. Chen, C. Zhao, Ultrathin metal-organic framework array for efficient electrocatalytic water splitting, *Nat. Commun.* 8 (2017) 15341, <https://doi.org/10.1038/ncomms15341>.
- [10] Z. Kou, L. Zhang, Y. Ma, X. Liu, W. Zang, J. Zhang, S. Huang, Y. Du, A.K. Cheetham, J. Wang, 2D carbide nanomeshes and their assembling into 3D microflowers for efficient water splitting, *Appl. Catal. B-Environ.* 243 (2019) 678–685, <https://doi.org/10.1016/j.apcatb.2018.11.008>.
- [11] H. Zou, B. He, P. Kuang, J. Yu, K. Fan, Ni<sub>3</sub>S<sub>2</sub> nanowalls/nitrogen-doped graphene foam is an efficient trifunctional catalyst for unassisted artificial photosynthesis, *Adv. Funct. Mater.* 28 (2018) 1706917, <https://doi.org/10.1002/adfm.201706917>.
- [12] K. Fan, H. Chen, Y. Ji, H. Huang, P.M. Claesson, Q. Daniel, B. Philippe, H. Rensmo, F. Li, Y. Luo, L. Sun, Nickel-vanadium monolayer double hydroxide for efficient electrochemical water oxidation, *Nat. Commun.* 7 (2016) 11981, <https://doi.org/10.1038/ncomms11981>.
- [13] X. Xu, H. Liang, F. Ming, Z. Qi, Y. Xie, Z. Wang, Prussian blue analogues derived penroseite (Ni<sub>3</sub>Co)Se<sub>2</sub> nanocages anchored on 3D graphene aerogel for efficient water splitting, *ACS Catal.* 7 (2017) 6394–6399, <https://doi.org/10.1021/acscatal.7b02079>.
- [14] K. Fan, Y. Ji, H. Zou, J. Zhang, B. Zhu, H. Chen, Q. Daniel, Y. Luo, J. Yu, L. Sun, Hollow iron-vanadium composite spheres: a highly efficient iron-based water oxidation electrocatalyst without the need for nickel or cobalt, *Angew. Chem. Int. Ed.* 56 (2017) 3289, <https://doi.org/10.1002/anie.201611863>.
- [15] H. Zou, B. He, P. Kuang, J. Yu, K. Fan, Metal-organic framework-derived nickel-cobalt sulfide on ultrathin MXene nanosheets for electrocatalytic oxygen evolution, *ACS Appl. Mater. Interfaces* 10 (2018) 22311–22319, <https://doi.org/10.1021/acsami.8b06272>.
- [16] Q. Che, Q. Li, Y. Tan, X. Chen, X. Xu, Y. Chen, One-step controllable synthesis of amorphous (Ni-Fe)<sub>x</sub>/NiFe(OH)<sub>2</sub> hollow microtube/sphere films as superior bifunctional electrocatalysts for quasi-industrial water splitting at large-current-density, *Appl. Catal. B-Environ.* 246 (2019) 337–348, <https://doi.org/10.1016/j.apcatb.2019.01.082>.
- [17] S.A. Rasaki, B. Zhang, K. Anbalgam, T. Thomas, M. Yang, Synthesis and application of nano-structured metal nitrides and carbides: a review, *Prog. Solid State Chem.* 50 (2018) 1–15, <https://doi.org/10.1016/j.progsolidstchem.2018.05.001>.
- [18] X. Zhang, R.-M. Kong, H. Du, L. Xia, F. Qu, Highly efficient electrochemical ammonia synthesis via nitrogen reduction reactions on a VN nanowire array under ambient conditions, *Chem. Commun.* 54 (2018) 5323–5325, <https://doi.org/10.1039/c8cc00459e>.
- [19] Z. Kou, T. Wang, Q. Gu, M. Xiong, L. Zheng, X. Li, Z. Pan, H. Chen, F. Verpoort, A.K. Cheetham, S. Mu, J. Wang, Rational design of holey 2D nonlayered transition metal carbide/nitride heterostructure nanosheets for highly efficient water oxidation, *Adv. Energy Mater.* 9 (2019) 1803768, <https://doi.org/10.1002/aenm.201803768>.
- [20] S. Dutta, A. Indra, Y. Feng, H. Han, T. Song, Promoting electrocatalytic overall water splitting with nanohybrid of transition metal nitride-oxynitride, *Appl. Catal. B-Environ.* 241 (2019) 521–527, <https://doi.org/10.1016/j.apcatb.2018.09.061>.
- [21] A. Jena, R.-X. Ye, H. Chang, T.-F. Hung, W.-S. Chang, R.-S. Liu, Synergistic improvement in charge overpotential of Li-O<sub>2</sub> batteries by oxidized carbon nanotubes and cobalt nitride composites, *J. Phys. Chem. C* 122 (2018) 13416–13423, <https://doi.org/10.1021/acs.jpcc.7b1172>.
- [22] T. Liu, M. Li, L. Guo, Designing and facilely synthesizing a series of cobalt nitride (Co<sub>3</sub>N) nanocatalysts as non-enzymatic glucose sensors: a comparative study toward the influences of material structures on electrocatalytic activities, *Talanta* 181 (2018) 154–164, <https://doi.org/10.1016/j.talanta.2017.12.082>.
- [23] C. Ray, S.C. Lee, B. Jin, A. Kundu, J.H. Park, S.C. Jun, Conceptual design of three-dimensional CoN/Ni<sub>3</sub>N-coupled nanograsses integrated on N-doped carbon to serve as efficient and robust water splitting electrocatalysts, *J. Mater. Chem. A* 6 (2018) 4466–4476, <https://doi.org/10.1039/c7ta10933d>.
- [24] M. Hojamberdiev, H. Wagata, K. Yubuta, K. Kawashima, J.J.M. Vequizo, A. Yamakata, S. Oishi, K. Domen, K. Teshima, KCl flux-induced growth of isometric crystals of cadmium-containing early transition-metal (Ti<sup>4+</sup>, Nb<sup>5+</sup>, and Ta<sup>5+</sup>) oxides and nitridability to form their (oxy) nitride derivatives under an NH<sub>3</sub> atmosphere for water splitting application, *Appl. Catal. B-Environ.* 182 (2016) 626–635, <https://doi.org/10.1016/j.apcatb.2015.10.002>.
- [25] P. Chen, K. Xu, Z. Fang, Y. Tong, J. Wu, X. Lu, X. Peng, H. Ding, C. Wu, Y. Xie, Metallic Co<sub>3</sub>N porous nanowire arrays activated by surface oxidation as electrocatalysts for the oxygen evolution reaction, *Angew. Chem. Int. Ed.* 54 (2015) 14710–14714, <https://doi.org/10.1002/anie.201506480>.
- [26] Y. Tong, X. Yu, H. Wang, B. Yao, C. Li, G. Shi, Trace level Co-N doped graphite foams as high-performance self-standing electrocatalytic electrodes for hydrogen and oxygen evolution, *ACS Catal.* 8 (2018) 4637–4644, <https://doi.org/10.1021/acscatal.8b01131>.
- [27] N. Wang, L. Li, D. Zhao, X. Kang, Z. Tang, S. Chen, Graphene composites with cobalt sulfide: efficient trifunctional electrocatalysts for oxygen reversible catalysis and hydrogen production in the same electrolyte, *Small* 13 (2017) 1701025, <https://doi.org/10.1002/smll.201701025>.
- [28] Y. Liu, S. Jiang, S. Li, L. Zhou, Z. Li, J. Li, M. Shao, Interface engineering of (Ni, Fe) S<sub>2</sub>/MoS<sub>2</sub> heterostructures for synergistic electrochemical water splitting, *Appl. Catal. B-Environ.* 247 (2019) 107–114, <https://doi.org/10.1016/j.apcatb.2019.01.094>.
- [29] X.-F. Lu, L.-F. Gu, J.-W. Wang, J.-X. Wu, P.-Q. Liao, G.-R. Li, Bimetal-organic framework derived CoFe<sub>2</sub>O<sub>4</sub>/C porous hybrid nanorod arrays as high-performance electrocatalysts for oxygen evolution reaction, *Adv. Mater.* 29 (2017) 1604437, <https://doi.org/10.1002/adma.201604437>.
- [30] T. Wang, Z. Kou, S. Mu, J. Liu, D. He, I.S. Amiinu, W. Meng, K. Zhou, Z. Luo, S. Chaemchuen, F. Verpoort, 2D dual-metal zeolitic-imidazolate-framework-(ZIF)-derived bifunctional air electrodes with ultrahigh electrochemical properties for rechargeable zinc-air batteries, *Adv. Funct. Mater.* 28 (2018) 1705048, <https://doi.org/10.1002/adfm.201705048>.
- [31] P. He, X.-Y. Yu, X.W. Lou, Carbon-incorporated nickel-cobalt mixed metal phosphide nanoboxes with enhanced electrocatalytic activity for oxygen evolution, *Angew. Chem. Int. Ed.* 56 (2017) 3897–3900, <https://doi.org/10.1002/anie.201612635>.
- [32] J. Liu, C. Wu, D. Xiao, P. Kopold, L. Gu, P.A. van Aken, J. Maier, Y. Yu, MOF-derived hollow Co<sub>9</sub>S<sub>8</sub> nanoparticles embedded in graphitic carbon nanocages with superior Li-ion storage, *Small* 12 (2016) 2354–2364, <https://doi.org/10.1002/smll.201503821>.
- [33] J. Sheng, L. Wang, L. Deng, M. Zhang, H. He, K. Zeng, F. Tang, Y.-N. Liu, MOF-templated fabrication of hollow Co<sub>3</sub>N@N-doped carbon porous nanocages with superior catalytic activity, *ACS Appl. Mater. Interfaces* 10 (2018) 7191–7200, <https://doi.org/10.1021/acsami.8b00573>.
- [34] B.Y. Guan, X.Y. Yu, H.B. Wu, X.W. Lou, Complex nanostructures from materials based on metal-organic frameworks for electrochemical energy storage and conversion, *Adv. Mater.* 29 (2017) 1703614, <https://doi.org/10.1002/adma.201703614>.
- [35] C. Qu, L. Zhang, W. Meng, Z. Liang, B. Zhu, D. Dang, S. Dai, B. Zhao, H. Tabassum, S. Gao, H. Zhang, W. Guo, R. Zhao, X. Huang, M. Liu, R. Zou, MOF-derived alpha-NiS nanorods on graphene as an electrode for high-energy-density supercapacitors, *J. Mater. Chem. A* 6 (2018) 4003–4012, <https://doi.org/10.1039/c7ta1100b>.
- [36] H. Zhang, W. Zhao, M. Zou, Y. Wang, Y. Chen, L. Xu, H. Wu, A. Cao, 3D, mutually embedded MOF@carbon nanotube hybrid networks for high-performance lithium-sulfur batteries, *Adv. Energy Mater.* 8 (2018) 1800013, <https://doi.org/10.1002/aenm.201800013>.
- [37] S.-K. Park, Y.C. Kang, MOF-templated N-doped carbon-coated CoSe<sub>2</sub> nanorods supported on porous CNT microspheres with excellent sodium-ion storage and electrocatalytic properties, *ACS Appl. Mater. Interfaces* 10 (2018) 17203–17213, <https://doi.org/10.1021/acsami.8b03607>.
- [38] J. Yang, G. Zhu, Y. Liu, J. Xia, Z. Ji, X. Shen, S. Wu, Fe<sub>3</sub>O<sub>4</sub>-decorated Co<sub>9</sub>S<sub>8</sub> nanoparticles in situ grown on reduced graphene oxide: a new and efficient

- electrocatalyst for oxygen evolution reaction, *Adv. Funct. Mater.* 26 (2016) 4712–4721, <https://doi.org/10.1002/adfm.201600674>.
- [39] P. Cai, J. Huang, J. Chen, Z. Wen, Oxygen-containing amorphous cobalt sulfide porous nanocubes as high-activity electrocatalysts for the oxygen evolution reaction in an alkaline/neutral medium, *Angew. Chem. Int. Ed.* 56 (2017) 4858–4861, <https://doi.org/10.1002/anie.201701280>.
- [40] W.D. Chemelewski, H.-C. Lee, J.-F. Lin, A.J. Bard, C.B. Mullins, Amorphous FeOOH oxygen evolution reaction catalyst for photoelectrochemical water splitting, *J. Am. Chem. Soc.* 136 (2014) 2843–2850, <https://doi.org/10.1021/ja411835a>.
- [41] R.D.L. Smith, M.S. Prevot, R.D. Fagan, Z. Zhang, P.A. Sedach, M.K.J. Siu, S. Trudel, C.P. Berlinguette, Photochemical route for accessing amorphous metal oxide materials for water oxidation catalysis, *Science* 340 (2013) 60–63, <https://doi.org/10.1126/science.1233638>.
- [42] T. Liu, Q. Liu, A.M. Asiri, Y. Luo, X. Sun, An amorphous CoSe film behaves as an active and stable full water-splitting electrocatalyst under strongly alkaline conditions, *Chem. Commun.* 51 (2015) 16683–16686, <https://doi.org/10.1039/c5cc06892d>.
- [43] P. Zhang, L. Li, D. Nordlund, H. Chen, L. Fan, B. Zhang, X. Sheng, Q. Daniel, L. Sun, Dendritic core-shell nickel-iron-copper metal/metal oxide electrode for efficient electrocatalytic water oxidation, *Nat. Commun.* 9 (2018) 381, <https://doi.org/10.1038/s41467-017-02429-9>.
- [44] C. Hu, J. Xue, L. Dong, Y. Jiang, X. Wang, L. Qu, L. Dai, Scalable preparation of multifunctional fire-retardant ultralight graphene foams, *ACS Nano* 10 (2016) 1325–1332, <https://doi.org/10.1021/acs.nano.5b06710>.
- [45] Z. Kou, T. Meng, B. Guo, I.S. Amiinu, W. Li, J. Zhang, S. Mu, A generic conversion strategy: from 2D metal carbides ( $M_xC_y$ ) to M-self-doped graphene toward high-efficiency energy applications, *Adv. Funct. Mater.* 27 (2017) 1604904, <https://doi.org/10.1002/adfm.201604904>.
- [46] T. Varga, G. Ballai, L. Vasarhelyi, H. Haspel, A. Kukovecz, Z. Konya, Co<sub>4</sub>N/nitrogen-doped graphene: a non-noble metal oxygen reduction electrocatalyst for alkaline fuel cells, *Appl. Catal. B-Environ.* 237 (2018) 826–834, <https://doi.org/10.1016/j.apcatb.2018.06.054>.
- [47] Z. Kou, T. Meng, B. Guo, I.S. Amiinu, W. Li, J. Zhang, S. Mu, A generic conversion strategy: from 2D metal carbides ( $M_xC_y$ ) to M-self-doped graphene towards high-efficiency energy applications, *Adv. Funct. Mater.* 27 (2017) 1604904, <https://doi.org/10.1002/adfm.201604904>.
- [48] X. Zheng, J. Wu, X. Cao, J. Abbott, C. Jin, H. Wang, P. Strasser, R. Yang, X. Chen, G. Wu, N-, P-, and S-doped graphene-like carbon catalysts derived from onium salts with enhanced oxygen chemisorption for Zn-air battery cathodes, *Appl. Catal. B-Environ.* 241 (2019) 442–451, <https://doi.org/10.1016/j.apcatb.2018.09.054>.
- [49] S. Dou, L. Tao, J. Huo, S. Wang, L. Dai, Etched and doped Co<sub>9</sub>S<sub>8</sub>/graphene hybrid for oxygen electrocatalysis, *Energy Environ. Sci.* 9 (2016) 1320–1326, <https://doi.org/10.1039/c6ee00054a>.
- [50] Z.-H. Sheng, L. Shao, J.-J. Chen, W.-J. Bao, F.-B. Wang, X.-H. Xia, Catalyst-free synthesis of nitrogen-doped graphene via thermal annealing graphite oxide with melamine and its excellent electrocatalysis, *ACS Nano* 5 (2011) 4350–4358, <https://doi.org/10.1021/nn103584t>.
- [51] Y. Zhao, R. Nakamura, K. Kamiya, S. Nakanishi, K. Hashimoto, Nitrogen-doped carbon nanomaterials as non-metal electrocatalysts for water oxidation, *Nat. Commun.* 4 (2013) 2390, <https://doi.org/10.1038/ncomms3390>.
- [52] J. Meng, C. Niu, L. Xu, J. Li, X. Liu, X. Wang, Y. Wu, X. Xu, W. Chen, Q. Li, Z. Zhu, D. Zhao, L. Mai, General oriented formation of carbon nanotubes from metal-organic frameworks, *J. Am. Chem. Soc.* 139 (2017) 8212, <https://doi.org/10.1021/jacs.7b01942>.
- [53] Y.-Z. Chen, C. Wang, Z.-Y. Wu, Y. Xiong, Q. Xu, S.-H. Yu, H.-L. Jiang, From bimetallic metal-organic framework to porous carbon: high surface area and multi-component active dopants for excellent electrocatalysis, *Adv. Mater.* 27 (2015) 5010–5016, <https://doi.org/10.1002/adma.201502315>.
- [54] Y. Zhang, B. Ouyang, J. Xu, G. Jia, S. Chen, R.S. Rawat, H.J. Fan, Rapid synthesis of cobalt nitride nanowires: highly efficient and low-cost catalysts for oxygen evolution, *Angew. Chem. Int. Ed.* 55 (2016) 8670–8674, <https://doi.org/10.1002/anie.201604372>.
- [55] Z. Li, M. Shao, L. Zhou, R. Zhang, C. Zhang, M. Wei, D.G. Evans, X. Duan, Directed growth of metal-organic frameworks and their derived carbon-based network for efficient electrocatalytic oxygen reduction, *Adv. Mater.* 28 (2016) 2337–2344, <https://doi.org/10.1002/adma.201505086>.
- [56] H. Cheng, M.-L. Li, C.-Y. Su, N. Li, Z.-Q. Liu, Cu-Co bimetallic oxide quantum dot decorated nitrogen-doped carbon nanotubes: a high-efficiency bifunctional oxygen electrode for Zn-air batteries, *Adv. Funct. Mater.* 27 (2017) 1701833, <https://doi.org/10.1002/adfm.201701833>.
- [57] X. Guo, C. Qian, R. Shi, W. Zhang, F. Xu, S. Qian, J. Zhang, H. Yang, A. Yuan, T. Fan, Fe<sub>2</sub>N/S/N codecorated hierarchical porous carbon nanosheets for trifunctional electrocatalysis, *Small* 15 (2019) e1804855, <https://doi.org/10.1002/sml.201803500>.
- [58] O. Mabayoje, A. Shoola, B.R. Wygant, C.B. Mullins, The role of anions in metal chalcogenide oxygen evolution catalysis: electrodeposited thin films of nickel sulfide as "pre-catalysts", *ACS Energy Lett.* 1 (2016) 195–201, <https://doi.org/10.1021/acsenenergylett.6b00084>.
- [59] L. Zhao, B. Dong, S. Li, L. Zhou, L. Lai, Z. Wang, S. Zhao, M. Han, K. Gao, M. Lu, X. Xie, B. Chen, Z. Liu, X. Wang, H. Zhang, H. Li, J. Liu, H. Zhang, X. Huang, W. Huang, Interdiffusion reaction-assisted hybridization of two-dimensional metal-organic frameworks and Ti<sub>3</sub>C<sub>2</sub>T<sub>x</sub> nanosheets for electrocatalytic oxygen evolution, *ACS Nano* 11 (2017) 5800–5807, <https://doi.org/10.1021/acs.nano.7b01409>.
- [60] T. Meng, J. Qin, S. Wang, D. Zhao, B. Mao, M. Cao, In situ coupling of Co<sub>0.85</sub>Se and N-doped carbon via one-step selenization of metal-organic frameworks as a trifunctional catalyst for overall water splitting and Zn-air batteries, *J. Mater. Chem. A* 5 (2017) 7001–7014, <https://doi.org/10.1039/c7ta01453h>.
- [61] T. Meng, Y.-N. Hao, L. Zheng, M. Cao, Organophosphoric acid-derived CoP quantum dots@S,N-codoped graphite carbon as a trifunctional electrocatalyst for overall water splitting and Zn-air batteries, *Nanoscale* 10 (2018) 14613–14626, <https://doi.org/10.1039/c8nr03299h>.
- [62] W. Zhao, T. Xu, T. Li, Y. Wang, H. Liu, J. Feng, S. Ding, Z. Li, M. Wu, Amorphous iron (III)-borate nanolattices as multifunctional electrodes for self-driven overall water splitting and rechargeable zinc-air battery, *Small* 14 (2018) 1802829, <https://doi.org/10.1002/sml.201802829>.
- [63] Y. Hao, Y. Xu, W. Liu, X. Sun, Co/CoP embedded in a hairy nitrogen-doped carbon polyhedron as an advanced tri-functional electrocatalyst, *Mater. Horiz.* 5 (2018) 108–115, <https://doi.org/10.1039/c7mh00706j>.